Chapter 2

Experimental methods

In this dissertation the magnetic structures of thin and ultrathin heavy lanthanide-metal films were investigated. Commonly used methods to characterize periodic structures are diffraction (or more general scattering) techniques, like neutron or x-ray scattering. Neutron scattering has played the leading role in the past to investigate magnetic structures in solids. Since the availability of synchrotron radiation sources also magnetic x-ray scattering became a powerful tool to probe magnetic structures. Furthermore, synchrotron radiation allows resonant scattering by tuning the photon energy to an absorption threshold, which leads to an element-specific enhancement of the scattering cross section. As will be shown in this work, resonant scattering is therefore well-suited to study thin films. The data presented in this dissertation were obtained by x-ray scattering and resonant magnetic x-ray scattering at conventional and soft x-ray energies. The latter technique is a very recent development and is applied in this dissertation for the first time to study AFM structures in thin films. As it will turn out, scattering in the soft x-ray region opens up new possibilities for the investigation of magnetic structures.

This chapter deals with basic aspects of x-ray scattering and magnetic x-ray scattering on and off resonance. Because multiple scattering effects are usually small in x-ray scattering, some points of this chapter will be discussed in a kinematical approximation. The specific properties of resonant soft x-ray scattering have been worked out in the present study and are discussed separately in detail in chapter 4.

2.1   X-ray scattering

When x-rays interact with matter, they can be absorbed or scattered, either elastically or inelastically. The elastic scattering processes are coherent and lead to a diffraction pattern. Elastic scattering can be satisfactorily described by classical electrodynamic theory with some quantum-mechanical modifications [65]. In a classical picture, the electrons of the target are accelerated by the incoming electromagnetic plane wave and reradiate at the same wavelength λ essentially with a dipole characteristic. The diffraction pattern of an arbitrary electron distribution can be calculated as the sum of waves emitted by electrons

of the target taking into account the phase difference caused by the different path lengths. The scattering amplitude A can be expressed as an integral over the sample volume [66]

$$A = -r_0 P \cdot \int \rho\left(\underline{r}\right) e^{\frac{2\pi i}{\lambda}\left(\widehat{s}-\widehat{s}_0\right)\cdot\underline{r}} d\underline{r}, \tag{2.1}$$

where $-r_0$ is the scattering amplitude of a free electron, P arises from the projection of the polarization vectors of incoming and scattered light, $\rho(\underline{r})$ is the electron density distribution, $\widehat{s}_0$ denotes the unit vector in the direction of the incoming light and $\widehat{s}$ the one in the direction of observation. The measured intensity is given by $|A|^2$.

In case of a crystalline solid, the periodic structure can be used to express the scattering amplitude [67]

$$A\left(\underline{q}\right) = -r_0 P \cdot \sum_{\underline{r}_j} f_j\left(\underline{q}, h\nu\right) e^{i\underline{q}\underline{r}_j} \sum_{\underline{R}_n} e^{i\underline{q}\underline{R}_n}, \tag{2.2}$$

where $\underline{q} = 2\pi(\widehat{s} - \widehat{s}_0)/\lambda$ is the scattering vector. The first sum covers one unit cell and is called the *unit-cell structure factor*, which is the sum over all atoms within the unit cell with the respective atomic *form factors* f_j and corresponding phase factors. The second sum goes over all lattice sites $\underline{R}_n$ and will be denoted by $F(\underline{q})$. For a crystal with a one-atomic basis, the scattering amplitude 2.2 simplifies to $A(\underline{q}) = -r_0 P \cdot f(\underline{q}, h\nu) \cdot F(\underline{q})$. The atomic form factor f is in general a complex number

$$f(\underline{q}, h\nu) = f^0(\underline{q}) + f'(h\nu) + i \cdot f''(h\nu), \tag{2.3}$$

with the Thomson term f^0, which depends on the momentum transfer $\underline{q}$ if the x-ray wavelength is of the order of the spatial extent of the electrons within the atom. $f'(h\nu)$ and $f''(h\nu)$ are the real and imaginary parts of the dispersion correction, which get important essentially at resonance energies [67].

The structure factor $F(\underline{q})$ for a finite crystal of $N_1 \times N_2 \times N_3$ unit cells can be described by the sum over all phase factors with lattice parameters a_i and components of the momentum transfer q_i [68]

$$\left|F\left(\underline{q}\right)\right|^2 = \left|\sum_{j_1=1}^{N_1}\sum_{j_2=1}^{N_2}\sum_{j_3=1}^{N_3} e^{i(q_1 a_1 j_1 + q_2 a_2 j_2 + q_3 a_3 j_3)}\right|^2 = \frac{\prod_{i=1}^{3}\sin^2\left(\frac{1}{2}N_i q_i a_i\right)}{\prod_{i=1}^{3}\sin^2\left(\frac{1}{2}q_i a_i\right)}. \tag{2.4}$$

When N_1, N_2, and N_3 are large numbers, the function is sharply peaked at the Bragg points with a peak intensity of $(N_1 N_2 N_3)^2$. The three Laue conditions for this are $q_1 a_1 = 2\pi h$, $q_2 a_2 = 2\pi k$, and $q_3 a_3 = 2\pi l$ (h, k, l integers) [68].

Scattering from thin-films and surfaces

In a real scattering experiment, the scattering volume is always limited by the size and penetration depth of the x-ray beam. While these boundaries are gradual, the boundaries formed by surfaces and interfaces are usually abrupt. If the crystal is finite, the scattered
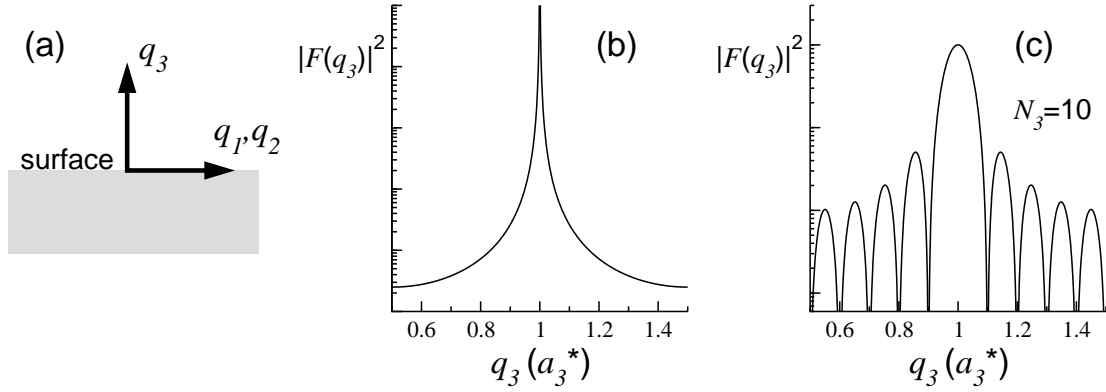
Figure 2.1: Simulations of equations 2.5 and 2.6 representing the crystal-truncation rods of a semi infinite crystal (b) and of a thin film (c) in reciprocal lattice units. The sketch in (a) defines the directions in momentum space.

intensity will be more and more distributed in reciprocal space with decreasing the size of the crystal.

A crystal with a surface can be thought of as a lattice which is laterally infinite and semi-infinite in the third direction. Carrying out the summation in equation 2.4 at a point in reciprocal space where the two in-plane Laue conditions are fulfilled, but not the third one for the direction normal to the surface plane, leads to [67, 68]:

$$|F(q_3)|^2 = \frac{N_1^2 N_2^2}{4 \sin^2\left(\frac{1}{2} q_3 a_3\right)}, \tag{2.5}$$

which is defined away from the Bragg peaks, i.e. if the denominator is $\neq 0$. This equation shows that there is finite intensity distributed along the surface normal, the so called *crystal-truncation rod* (CTR). Figure 2.1 (b) shows the shape of the CTR on a logarithmic scale according to equation 2.5; q_3 is given in reciprocal lattice units in direction perpendicular to the surface (a_3^*). It is worth to note that the scattered intensity away from the Bragg peak is of the same order as the intensity scattered from a single monolayer [68]. It can be shown that the intensity distribution along the CTR depends strongly on the properties of the surface e.g. surface roughness and layer spacing [67–69]. Therefore, measurements of CTR's have become a useful probe of the surface structure and the near-surface region of single crystals. The shape of the CTR is also determined by e.g. a finite penetration depth and a finite coherence length of the x-rays.

A second case, important for this dissertation, is the scattering from a thin film. This is approximated by a laterally infinite lattice, with a finite number of scattering planes in the third direction. The diffraction pattern perpendicular to the surface derived from equation 2.4 is given by the Laue function [68]

$$|F(q_3)|^2 = N_1^2 N_2^2 \frac{\sin^2\left(\frac{1}{2} N_3 q_3 a_3\right)}{\sin^2\left(\frac{1}{2} q_3 a_3\right)}. \tag{2.6}$$
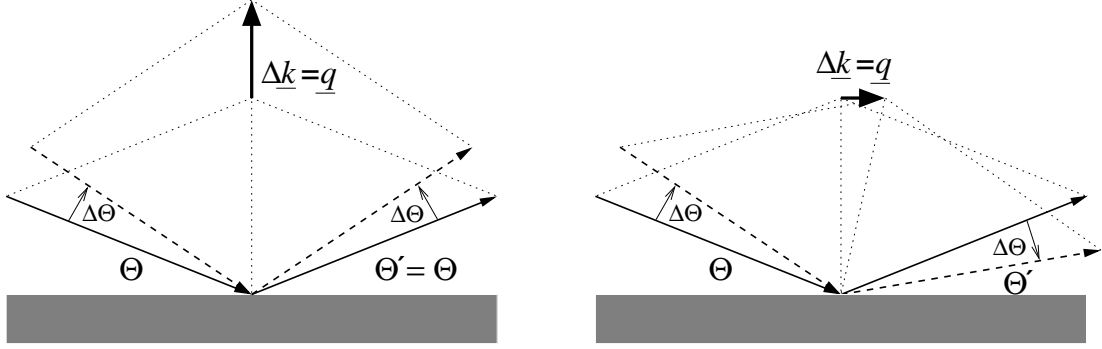
Figure 2.2: Typical scans in reciprocal space used in the present work. Left: longitudinal scan (specular geometry). Right: transverse or rocking scan probing the off-specularly scattered intensity.

This function is plotted in figure 2.1 (c) for the case of a 10-layer-thick film. The number of layers, N_3, determines both the width of the Bragg peak and the distance to the side maxima, the so-called Laue oscillations.

Typical scans in reciprocal space

The diffraction pattern of a crystal is three-dimensional. In case of a thin film, there are two naturally distinct directions; perpendicular to the sample surface, where the sample is of finite size and parallel to the surface, where the sample is practically infinite. The scans that correspond to these directions and that are used in the present work are called *longitudinal* and *transverse* scans, depending on the rotations of sample and detector.

A longitudinal scan is shown schematically on the left side of figure 2.2. If the angles of the incident and detected x-rays are equal with respect to the sample surface (specular geometry), the scattering vector is perpendicular to the sample surface ($q_\perp$). A simultaneous change of detector and sample angle in specular geometry results in a longitudinal scan. Since the angles of incidence Θ and detection Θ' are equal in specular geometry, they will be denoted as $\widetilde{\Theta}$ in the following.

An example of a longitudinal scan from a thin film on a substrate is given in figure 2.3. It shows the scattering pattern of a 27-monolayer-thick (ML) Ho film along the specular (00l) direction on a logarithmic scale. The component of the scattering vector along the c^* direction of the reciprocal lattice is usually denoted by L. In the present case, the lanthanide metal films are (0001) oriented and so $q_\perp = L$. In figure 2.3, the length of the scattering vector is given in reciprocal lattice units c^*. For specular geometry, the relation between the scattering angle $\widetilde{\Theta}$ and the scattering vector is given by

$$q_\perp = L = \frac{4\pi}{\lambda} \sin \widetilde{\Theta}, \qquad L/c^* = \frac{2c}{\lambda} \sin \widetilde{\Theta},$$

with the x-ray wavelength λ and the reciprocal lattice parameter c^*[1]. The upper panel of

---

[1]Throughout this thesis, the reciprocal lattice parameters are calculated from the room temperature

figure 2.3 displays the crystal-truncation rod of the uncovered W(110) substrate along the surface normal. The intensity distribution of the W rod in reciprocal space is characteristic for a semi infinite crystal (figure 2.1 (b)), with scattered intensity even far away from the Bragg-peak position.

The lower panel in figure 2.3 displays the same kind of scan from a Ho film grown on the W substrate. At small scattering vectors, the so called *Kiessig fringes* [70] can be observed arising from interference of x-rays reflected from the Ho surface and from the Ho/W interface. In an hcp lattice, the first Bragg peak along the $(00l)$ direction appears at $L = 2c^*$ corresponding to the single layer spacing that is half of the $c-$axis lattice parameter. The intensity of the Bragg peak is distributed over a large volume in momentum space and shows characteristic side maxima and minima called Laue oscillations. The intensity distribution can be nicely described by equation 2.6 plus an additional background arising from the CTR of the W substrate. The Kiessig fringes and Laue oscillations are of different origin and contain complementary information about film thickness and roughness. Kiessig fringes are not sensitive to the atomic structure and can also be observed in liquid films [71] or from polycrystalline layered materials [72], while the Laue oscillations are related to the crystalline structure. From the Kiessig fringes, the total film thickness can be determined, while the Laue oscillations give information about the number of coherently scattering lattice planes. If both numbers agree, as in case of the spectrum in figure 2.3, the film is single-crystalline throughout its whole thickness.

Information on in-plane correlations can be obtained from a transverse or rocking scan, as shown schematically on the right side of figure 2.2. Rotating the sample through the specular position with the detector kept fixed leads to a variation of the momentum transfer essentially parallel to the surface ($q_\parallel$). For small deviations from specular geometry, this path can be approximated by a straight line in momentum space perpendicular to the $q_\perp$ direction. The in-plane momentum transfer, $q_\parallel$, and the width of the transverse scan, $\Delta q_\parallel$, are given by

$$q_\parallel = \frac{2\pi}{\lambda} \left(\cos\left(2\widetilde{\Theta} - \Theta\right) - \cos\left(\Theta\right) \right), \qquad \Delta q_\parallel = \frac{4\pi}{\lambda} \sin\left(\widetilde{\Theta}\right) \cdot \Delta\Theta,$$

where Θ is the angle between the surface and the incident x-rays and $2\widetilde{\Theta} - \Theta$ is the angle of observation. The transverse scan probes the extension of the Bragg peaks parallel to the surface and by that, it is a probe of the in-plane coherence. Since real single crystals are often composed of small, ideal crystal grains, also called mosaic blocks, the rocking width is related to their size and orientation distribution. Thus, the rocking width of a structural Bragg reflection is often called mosaic spread and reflects essentially the quality of the crystal.

The transverse scan at the Ho(002) Bragg-peak position is shown in the inset of figure 2.3. The rocking width found here is considerably better than those reported for MBE grown Ho films and comparable to good single crystals [73]. This example shows the best crystallinity achieved in our experiments. Typical rocking width were of the order of 0.06°, which is still very good for metal films.

---

lattice constants of Ho and Dy metal, $c = 5.618$ Å and 5.650 Å [5], respectively.
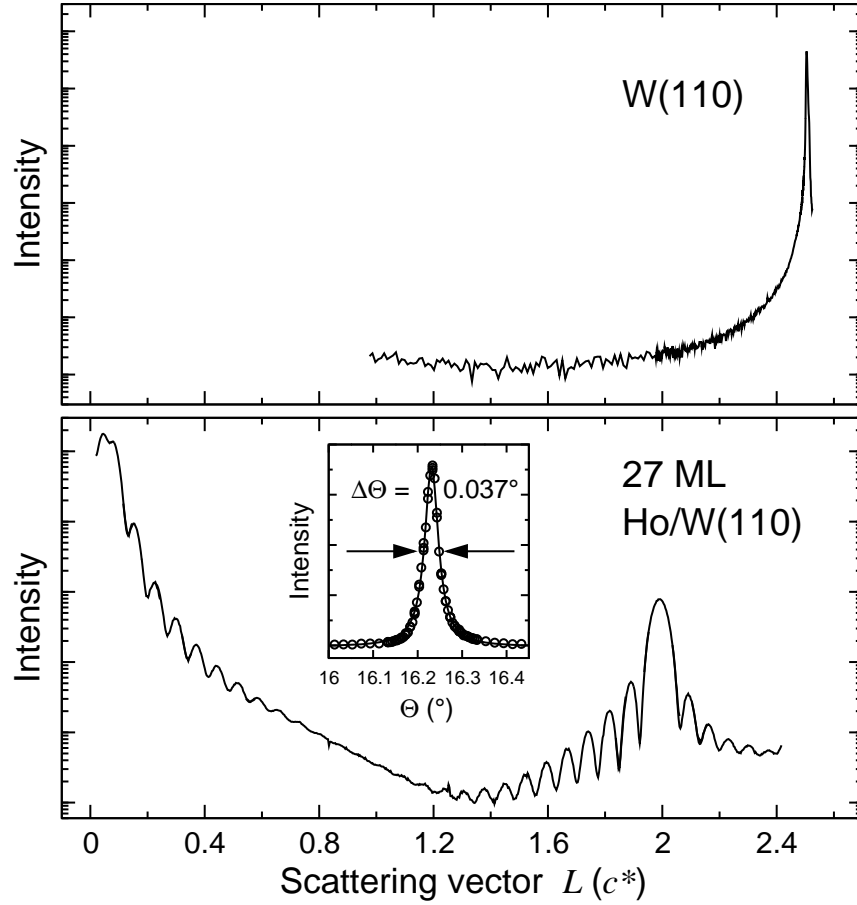
Figure 2.3: Upper panel: W(110) Bragg peak and the crystal-truncation rod along the (110) direction. Lower panel: specular reflectivity of a 27-ML Ho film epitaxially grown on a W(110) substrate, showing the Kiessig fringes at small scattering angles and the Ho(002) Bragg peak. The momentum transfer for both curves is given in Ho reciprocal lattice units. The inset shows a transverse scan at the Ho(002) Bragg-peak position.

X-ray reflectivity

For x-rays, the index of refraction $n = 1 - \delta + i\beta$ is usually close to unity, and the small deviation from unity can be neglected in many x-ray scattering experiments justifying the kinematical approach. But near grazing incidence, the reflected intensity depends sensitively on the change of the index of refraction at an interface, which can be seen directly from Snell's law. Due to this sensitivity and due to the comparably strong change of the optical constants δ and β at strong resonances, like the M_V absorption thresholds of the heavy lanthanide metals, it can become necessary to include dispersion corrections into the data analysis.

If an incident x-ray beam propagates from one medium into the other with different optical properties, it is required that the wave and its derivative at the surface and interface
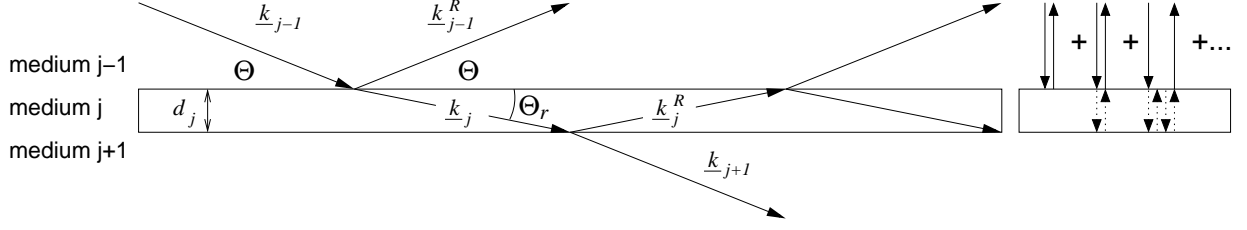
Figure 2.4: Reflection and transmission in a slab of finite thickness with sharp boundaries. $\underline{k}_j$ denotes the wave vector of the incident beam in slab j and $\underline{k}_j^R$ the corresponding wave vector of the beam reflected at the interface to slab $j+1$. This leads to the momentum transfer $q_j = |\underline{k}_j^R - \underline{k}_j|$. The total reflectivity is the sum of all possible reflection paths, as schematically shown in the right part.

are continuous. From these requirements, Snell's law and the Fresnel equations can be derived [67, 74]. An incident plane wave propagating at an angle Θ with respect to the interface splits into a specularly reflected wave at the same angle and a refracted wave at Θ_r, as shown in figure 2.4. As Θ and Θ_r are small, the cosines of Snell's law, $\cos\Theta = n\cos\Theta_r$, can be expanded to yield a corrected expression for the now complex momentum transfer within the absorbing medium

$$q' = \frac{4\pi}{\lambda} \cdot \sin\left(\sqrt{\widetilde{\Theta}^2 - 2\delta + i2\beta}\right),$$

where $\widetilde{\Theta}$ is defined as the scattering angle in specular geometry. From this, the reflectance from the surface of a semi-infinite crystal can be written as the complex quantity $r = (q - q')/(q + q')$. The reflected intensity, $I_R \propto |r|^2$, falls off rapidly with q^{-4} for scattering angles large compared to the critical angle $\Theta_C = \sqrt{2\delta}$ [75].

A general description of reflection from N stratified homogeneous slabs is given by Parratt [72]. The situation is sketched in figure 2.4. In this case, the evaluation of the boundary conditions leads to a recursive formula for the reflectance of the interface, $r_{j-1,j}$, between the jth and the $(j-1)^{th}$ slab

$$r_{j-1,j} = a_{j-1}^4 \left[\frac{r_{j,j+1} + F_{j-1,j}}{r_{j,j+1}F_{j-1,j} + 1}\right],$$

where $a_j = \exp(-iq_jd_j/4)$ is the phase factor and $F_{j-1,j} = (q_{j-1} - q_j)/(q_{j-1} + q_j)$ are the Fresnel coefficients for a reflection from the interface $j-1, j$, described by the complex momentum transfer q_j. Starting from the substrate slab N with infinite thickness and therefore with reflectance $r_{N-1,N} = a_{N-1}^4 F_{N-1,N}$, and defining the phase factor on the vacuum side $a_1 = 1$, the recursive solution leads to the intensity reflected from the surface

$$\frac{I_R}{I_0} = |r_{1,2}|^2,$$

with the incident intensity I_0.

So far, I described the theory for sharp interfaces. Since scattering at grazing angles is sensitive to the change of the index of refraction, it is sensitive to the exact electron-density profile at the surface and the interfaces of the sample. Thus, it is important to include surface and interface roughness into the model. The most simple expression can be derived in kinematical approximation, which describes the reflectivity by the Fourier transform of the electron-density profile perpendicular to the surface. While a sharp surface is described by an abrupt change of the electron-density profile, a rough surface with a height variation described by a Gaussian distribution of width σ_{rms} leads to a *Debye-Waller*-like damping of the reflected intensity [71, 75]

$$I_R = I_R^{Fresnel} e^{-q^2 \sigma_{rms}^2}.$$

The value of σ_{rms} (root-mean-square roughness) is conventionally used to express surface and interface roughness.

2.2   Magnetic x-ray scattering

The concepts discussed in the previous sections are in principle independent of the scattering mechanism, but the discussion so far has focused on the interaction between the electric field of the electromagnetic wave and the charge of the electron (equation 2.1). While charge scattering is the dominant mechanism, the electric and magnetic field of the x-ray also interact with the magnetic moments, which gives rise to magnetic scattering. The magnetic contribution to the scattering cross section was calculated for the first time by Gell-Mann and Goldberger [76]. Platzman and Tzoar calculated its dependence on the scattering vector and predicted that x-rays could be used to determine magnetic structures [77]. Magnetic x-ray scattering was for the first time experimentally observed in 1972 by de Bergevin and Brunel for AFM NiO [78]. This comparably late observation is due to the fact that the magnetic-scattering cross section is very small. Compared to the charge-scattering cross section, it is reduced by a factor of $(h\nu/m_0 c^2)^2$ for a single electron. For typical x-ray energies of 10 keV this factor is of the order of 10^{-4}. If x-rays are scattered by an atom, the magnetic-scattering cross section is further reduced as compared to charge scattering, because only unpaired electrons take part in the magnetic-scattering process. Thus, the magnetically scattered intensity is typically 5 to 6 orders of magnitude smaller than the charge scattering intensity.

Despite the small magnetic-scattering cross section, magnetic x-ray scattering made a fast progress with the routine availability of synchrotron radiation sources providing high photon flux. With the tunability of the photon energy of synchrotron radiation, the new technique of resonant (magnetic) x-ray scattering appeared, which makes use of the strong change of the scattering cross section near absorption thresholds. X-ray (magnetic) scattering should be considered within two regimes. One is the non-resonant limit with the photon energy well separated from an absorption threshold. The second is the resonant regime where the photon energy lies near an absorption threshold. Both methods have their own characteristics and contain slightly different information. Both techniques require the

use of synchrotron radiation. In the non-resonant limit for practical reasons, because the magnetic-scattering amplitude is very weak compared to that of charge scattering. Thus, it requires a high photon flux to get a reasonable counting rate. And since the magnetic-scattering process rotates the polarization direction of the x-rays, which can be used to separate magnetic from charge scattering contribution, magnetic scattering requires radiation with a high degree of polarization. In case of resonant magnetic scattering it is necessary to tune the photon energy across the resonance, which also requires to work at a synchrotron-radiation source.

Theoretical description of the magnetic-scattering process

This section describes the quantum mechanical basics of magnetic scattering. The description follows the treatment and the notation by *M. Blume* in reference 79.

The Hamiltonian of bound electrons coupled to an electromagnetic field is given by

$$\mathcal{H} = \sum_j \frac{1}{2m} \left(\underline{P}_j - \frac{e}{c} \underline{A} \left(\underline{r}_j \right) \right)^2 + \sum_{ij} V \left(\underline{r}_{ij} \right)$$

$$- \frac{e\hbar}{2mc} \sum_j \underline{s}_j \cdot \nabla \times \underline{A} \left(\underline{r}_j \right) - \frac{e\hbar}{2 \left(mc \right)^2} \sum_j \underline{s}_j \cdot \underline{E} \left(\underline{r}_j \right) \times \left(\underline{P}_j - \frac{e}{c} \underline{A} \left(\underline{r}_j \right) \right)$$

$$+ \sum_{\underline{k},\lambda} \hbar \omega_k \left(c^+ \left(\underline{k} \lambda \right) c \left(\underline{k} \lambda \right) + \frac{1}{2} \right).$$

Besides the familiar terms of the kinetic energy (canonical momentum in the presence of an electromagnetic field) and the potential energy, the third term describes the interaction of the magnetic part of the electromagnetic wave ($\underline{B} = \nabla \times \underline{A}$) with the spin of the electron $\underline{s}_j$ (Zeeman interaction). Term four is the spin-orbit term, where $\underline{E} = -\nabla \phi - 1/c \cdot d\underline{A}/dt$ is an effective electric field with the Coulomb potential ϕ. This term includes the ordinary spin-orbit coupling for electrons and a second spin-orbit term that can be thought of as the interaction of the electron spin with the magnetic part of the Lorentz-transformed electric field of the electromagnetic wave. And the last term describes the energy of the electromagnetic wave field expressed in photon creation and annihilation operators $c^+ \left(\underline{k} \lambda \right)$ and $c \left(\underline{k} \lambda \right)$.

This Hamiltonian can be split into the unperturbed system $\mathcal{H}_0$, a part describing the radiation field $\mathcal{H}_{rad.}$, and an interaction term $\mathcal{H}_{int.}$: $\mathcal{H} = \mathcal{H}_0 + \mathcal{H}_{rad.} + \mathcal{H}_{int.}$, with

$$\mathcal{H}_{int.} = \frac{e^2}{2mc^2} \sum_j \underline{A}^2 \left(\underline{r}_j \right) - \frac{e}{mc} \sum_j \underline{A} \left(\underline{r}_j \right) \cdot \underline{P}_j$$

$$- \frac{e\hbar}{mc} \sum_j \underline{s}_j \cdot \left[\nabla \times \underline{A} \left(\underline{r}_j \right) \right] - \frac{e\hbar}{2 \left(mc \right)^2} \frac{e^2}{c^2} \sum_j \underline{s}_j \cdot \left[\frac{d}{dt} \underline{A} \left(\underline{r}_j \right) \times \underline{A} \left(\underline{r}_j \right) \right]. \qquad (2.7)$$

A perturbational treatment to second order results in a cross section obtained from the transition probability given by the *golden rule*:

$$w = \frac{2\pi}{\hbar} \left| \langle f \, |\mathcal{H}_{int.}| \, i \rangle + \sum_n \frac{\langle f \, |\mathcal{H}_{int.}| \, n \rangle \langle n \, |\mathcal{H}_{int.}| \, i \rangle}{E_i - E_n} \right|^2 \delta \left(E_i - E_f \right), \qquad (2.8)$$

with the initial state $|i\rangle \equiv \left| \widetilde{i}; \underline{k}\lambda \right\rangle$, the final state $|f\rangle \equiv \left| \widetilde{f}; \underline{k'}\lambda' \right\rangle$, the intermediate states $|n\rangle$ and the corresponding energies $E_i = \widetilde{E}_i + \hbar\omega, \cdots$, including the photon $\underline{k}\lambda$.

Since the vector potential $\underline{A}$ is linear in photon creation and annihilation operators, scattering occurs only from contributions quadratic in $\underline{A}$, because scattering requires first an annihilation and a subsequent creation of a photon. Accordingly, the first term of the interaction Hamiltonian (2.7) leads to the usual Thomson scattering in first order. Also the fourth term is quadratic in $\underline{A}$ and describes spin-dependent scattering in first order. The second and third terms are linear in $\underline{A}$, thus scattering occurs in second order involving excitations into an intermediate state $|n\rangle$. This gives rise to resonant scattering with a huge contribution if the energy denominator in equation 2.8 becomes small close to resonance. The excitation of core electrons into intermediate states makes the scattering selective to the respective element and its chemical environment. Due to magnetic exchange splitting and spin polarization, resonant scattering is also sensitive to magnetism.

Non-resonant magnetic scattering

In the non-resonant limit, the magnetic-scattering amplitude has the simple form [80–83]

$$\widetilde{f}_{mag}^{nonres} \propto \frac{1}{2} \underline{L} \left(\underline{q} \right) \cdot \underline{A} + \underline{S} \left(\underline{q} \right) \cdot \underline{B}.$$

Here $\underline{L}(\underline{q})$ and $\underline{S}(\underline{q})$ denote the Fourier transforms of the orbital and spin magnetization densities, respectively. The matrices $\underline{A}$ and $\underline{B}$ act on the polarization vectors and depend on the wave vectors of the incoming and scattered light. The components can be chosen by the experimental geometry. There are two main aspects of the non-resonant magnetic-scattering amplitude. Firstly, $\underline{A}$ and $\underline{B}$ have non-diagonal elements. This means that a part of the magnetically scattered x-rays changes the polarization direction, which does not occur in charge scattering. Accordingly, polarization analysis of the scattered beam can discriminate the magnetic signal from the charge scattering. Secondly, $\underline{A}$ and $\underline{B}$ are not identical in contrast to magnetic neutron scattering. The difference in the polarization dependence leads to a difference in the scattering cross sections for the orbital and spin moment and can be used to separate these contributions, which is not directly possible with neutron scattering [82]. With the magnetic-scattering channel, the total elastic scattering amplitude is now $\widetilde{f} = \widetilde{f}_0 + \widetilde{f}' + i\widetilde{f}'' + \widetilde{f}_{mag}^{nonres}$ including the polarization dependence[2] so that $d\sigma/d\Omega = |\widetilde{f}|^2$.

---

[2]In magnetic scattering it is often useful to include the polarization dependence P into the atomic form factor f. To distinguish the quantity including P from f, it is denoted as $\widetilde{f}$ throughout this thesis.

Resonant magnetic scattering

Most of the scattering experiments in this work were carried out by exploiting resonances. At resonance, when the photon energy is tuned to an absorption threshold, there is an additional contribution $\widetilde{f}_{res}$ to the scattering amplitude. Within a simple one-electron picture, an incident photon promotes an inner-shell electron to an unoccupied state above the Fermi level. This excitation decays through emission of a scattered photon of the same energy.

As compared to non-resonant magnetic scattering, the resonant-scattering amplitude is more complicated. For electric dipole transitions $E1$, it was calculated by Hannon *et al.* [84], and can be written as the sum of three separate terms [83]:

$$\widetilde{f}_{res}^{E1}(h\nu) = \widetilde{f}_0(h\nu) + \widetilde{f}_{circ}(h\nu) + \widetilde{f}_{lin}(h\nu), \tag{2.9}$$

where

$$\widetilde{f}_0(h\nu) = -\left(\frac{3}{4\pi k}\right)(\widehat{\varepsilon}' \cdot \widehat{\varepsilon})\left[F_{+1}^1 + F_{-1}^1\right]$$

$$\widetilde{f}_{circ}(h\nu) = -i\left(\frac{3}{4\pi k}\right)(\widehat{\varepsilon}' \times \widehat{\varepsilon}) \cdot \widehat{m}\left[F_{-1}^1 - F_{+1}^1\right]$$

$$\widetilde{f}_{lin}(h\nu) = -\left(\frac{3}{4\pi k}\right)(\widehat{\varepsilon}' \cdot \widehat{m})(\widehat{\varepsilon} \cdot \widehat{m})\left[2F_0^1 - F_{+1}^1 - F_{-1}^1\right];$$

here, the F_ζ^1 are energy-dependent dimensionless resonant oscillator strengths for dipole transitions with a change in the magnetic quantum number ζ. The first term, $\widetilde{f}_0(h\nu)$, is independent of the local magnetic axis $\widehat{m}$. As in case of Thomson scattering it does not change the polarization direction, expressed as the inner product of the polarization vectors of the incoming and the scattered light, $\widehat{\varepsilon}$ and $\widehat{\varepsilon}'$. This leads to $\sigma \to \sigma'$ or $\pi \to \pi'$ scattering, where σ denotes the x-ray-polarization direction perpendicular and π parallel to the scattering plane spanned by the wave vectors of the incident and detected x-rays. This contribution is known as *anomalous scattering*. The second term depends on the difference in the resonant oscillator strengths, F_ζ^1, where ζ is the projection of the photon spin on the local magnetic axis $\widehat{m}$ (unit vector). With the selection rule for photon absorption $\zeta = \Delta M_J = \pm 1$, this term is of circular dichroic nature. After scattering, the polarization direction is rotated by a certain angle, leading to finite σ' or π' components in the scattered light ($\sigma \to \pi'$ or $\pi \to \sigma'$ scattering). The scattering amplitude contains $\widehat{m}$ as a linear term, leading to peaks at the same points in reciprocal space as from non-resonant scattering, which is linear in $\widehat{m}$ as well. The last term of the scattering amplitude is of linear dichroic nature. Since the projection on local magnetic axis appears twice, this contribution is quadratic in $\widehat{m}$.

The resonant $E2$ or electric quadrupole amplitude contains terms in $\widehat{m}$ from zero up to fourth order with 13 distinct contributions. Hence, $E2$ resonant scattering can contribute

to the main Bragg reflections and satellites up to the order of four [84]. As a result, the scattering amplitude is the coherent sum of contributions from $E1$, $E2$, . . . events. At strong dipole resonances like the $M_{IV,V}$ absorption thresholds of the lanthanides, the contributions from electric quadrupole or higher transitions are very weak as compared to $E1$ and can be neglected.

By tuning the photon energy to a resonance, an enhancement of the magnetic-scattering signal occurs if there is a difference in the cross section between spin-up and spin-down electronic states. This difference can arise in a number of ways making the identification of the responsible mechanism not as straightforward as in case of non-resonant scattering.

The first and most obvious reason is the finite spin polarization of the partially filled states into which the core electron is excited. If there are more unoccupied states of one spin direction than of the other, there is a higher transition probability to the first ones, leading to magnetic contrast in the scattering cross section. This in particular is the case for the $3d$ states of the $3d$-transition metals ($L_{II,III}$ absorption thresholds) and for the $4f$ and $5f$ states of lanthanides and actinides ($M_{IV,V}$ absorption thresholds), respectively, where a resonant enhancement of the magnetic-scattering signal can be expected.

A second possible reason for an enhanced magnetic signal lies in the difference of overlap integrals between spin-up and spin-down states. This arises from polarization via hybridization by another strongly polarized state [85]. Van Veenendaal *et al.* have found that the difference in the spatial extent of the spin-up and spin-down $5d$ states due to interaction with the strongly polarized $4f$ states makes a major contribution to the observed signal at the Ho $L_{II,III}$ thresholds. Excitation into polarized $5d$ states gives rise to a resonant enhancement of the magnetic signal by a factor of 50 as compared to off-resonant scattering. In fact, it was the L_{III} threshold of Ho at which the first discoveries of resonant magnetic scattering were made by Gibbs *et al.* [81].

Finally, if the resonant excitation energies, or the lifetimes of the spin-up and spin-down channels are different, there might also be a magnetic contrast, i.e. an enhancement of the magnetic signal can arise. In contrast to the situations described above, this can happen even with a totally empty intermediate state, where the assignment of a finite polarization in the valence shell might be incorrect [86]. Experimental evidence of this effect has been found at the K threshold of Mn in the orbitally-ordered material $LaMnO_3$ [87].

Scattering from helical-antiferromagnetic Ho

Caused by the different contributions to the resonant-scattering amplitude in equation 2.9, strong variations of the magnetic-scattering properties across an absorption threshold can be expected, like the polarization dependence and the magnetic-scattering intensity. While equation 2.9 holds for free atoms, for crystals one has to consider also the specific magnetic structure and the individual scattering geometry in order to compare equation 2.9 with the experimental results. In the following, resonant magnetic x-ray scattering will be illustrated for the case of Ho metal. As already mentioned in chapter 1, bulk Ho metal is a helical antiferromagnet between its Curie temperature of about 20 K and the Néel temperature of 131.2 K. The helical structure consists of ferromagnetically ordered moments in the basal
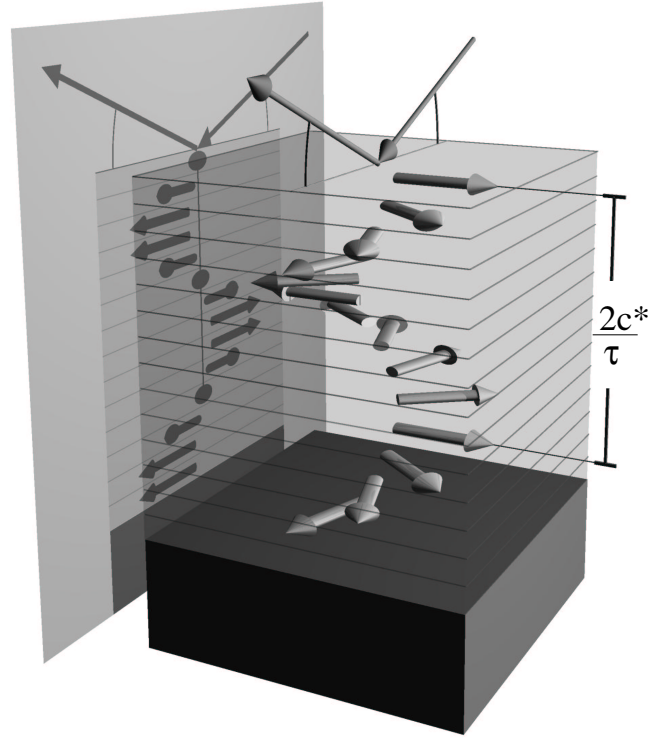
Figure 2.5: Helical AFM structure of a Ho-metal film with a magnetic period of $2c^*/\tau$. A projection of the magnetic moments of the helical structure onto the scattering plane results in a harmonic modulation.

planes of the hcp lattice with the moment of each plane rotated by a certain angle with respect to the neighboring plane, thus forming a helix along the crystallographic c axis, as shown schematically in figure 2.5. The magnetic period is temperature dependent with a length of about 10 monolayers at 40 K, decreasing with increasing temperature to about 7 monolayers at the Néel temperature [88]. Since Ho exhibits a nearly perfect helical magnetic structure, even in case of thin films, the interpretation of the scattering data is comparably simple, because no higher Fourier components of the magnetic structure exist and higher harmonics in the scattering signal are caused by the resonant-scattering process alone. The magnetic-scattering process depends on projections of the local magnetic axis. For the helical structure, the projection of the magnetic moments perpendicular to the helix propagation results in a sinusoidal modulation as illustrated in figure 2.5. Since the resonant-scattering amplitude (equation 2.9) consists of a part that is linear and one which is quadratic in the local magnetic axis $\widehat{m}$, a first and a second harmonic can be expected, corresponding to the period of the sine and the half period caused by the squared sine.

To describe diffraction from a helix in $\widehat{x}$ direction one has to introduce the magnetic structure factor [83]

$$\widehat{m} \rightarrow \sum_{\underline{R}_n} \exp\left(i\underline{Q} \cdot \underline{R}_n\right) \cdot \widehat{m}\left(\underline{R}_n\right),$$

with the position-dependent magnetic unit vector $\widehat{m}\left(\underline{r}\right)$ evaluated at the atomic coordinate $\underline{R}_n$

$$\widehat{m}\left(\underline{r}\right) = \widehat{y}\cos\left(\tau x\right) - \widehat{z}\sin\left(\tau x\right),$$

where τ is the absolute value of the magnetic modulation vector. With this replacement and by assuming a purely $\pi-$polarized incident x-ray beam (x-ray polarization vector parallel to the scattering plane as illustrated in figure 2.6), as used in most experiments of the present work, the scattering amplitude in dipole approximation can be written as the sum of zero-order (zo), first-order (fo), and second-order (so) harmonics corresponding to a series of magnetic-superstructure satellites separated by 0τ, $\pm1\tau$, and $\pm2\tau$ from the chemical Bragg reflections in momentum space, respectively [83]

$$\widetilde{f}_{helix,\pi}^{E1}\left(h\nu\right) = \widetilde{f}^{zo}\left(h\nu\right) + \widetilde{f}^{fo}\left(h\nu\right) + \widetilde{f}^{so}\left(h\nu\right),\qquad(2.10)$$

where

$$\widetilde{f}^{zo}(h\nu) = -\left(\frac{3}{4\pi k}\right)\left[\left[F_{+1}^1 + F_{-1}^1\right]\begin{pmatrix}0\\\cos\left(\vartheta\right)\end{pmatrix} + \left[2F_0^1 - F_{+1}^1 - F_{-1}^1\right]\begin{pmatrix}0\\-\frac{1}{2}\sin^2\left(\frac{\vartheta}{2}\right)\end{pmatrix}\right]$$

$$\widetilde{f}^{fo}(h\nu) = -\left(\frac{3}{4\pi k}\right)\left[F_{-1}^1 - F_{+1}^1\right]\begin{pmatrix}\frac{i}{2}\cos\left(\frac{\vartheta}{2}\right)\\\mp\frac{1}{2}\sin\left(\vartheta\right)\end{pmatrix}$$

$$\widetilde{f}^{so}(h\nu) = -\left(\frac{3}{4\pi k}\right)\left[2F_0^1 - F_{+1}^1 - F_{-1}^1\right]\begin{pmatrix}\pm\frac{i}{4}\sin\left(\frac{\vartheta}{2}\right)\\-\frac{1}{4}\sin^2\left(\frac{\vartheta}{2}\right)\end{pmatrix}.$$

In general, $\widetilde{f}_{helix}^{E1}$ is a second-order tensor in the σ (x-ray polarization vector perpendicular to the scattering plane) and π components of the incident x-ray beam and the σ' and π' components of the scattered x-rays. But choosing a fixed polarization direction for the incident x-rays, it reduces to a vector expression. The upper elements represent the $\pi \to \sigma'$, the lower elements the $\pi \to \pi'$ scattering contribution. The different polarization dependences in equation 2.9 lead to the different geometry factors, which are functions of the detection angle $\vartheta = 2\widetilde{\Theta}$ in specular scattering geometry.

As can be seen from equation 2.10, the direction of photon polarization is changed by magnetic scattering, while charge scattering does not affect the polarization. This can be exploited to discriminate magnetic from charge scattering by means of polarization analysis [89]. A schematic view of the scattering geometry in which most of the experiments in the conventional x-ray region were done is shown in figure 2.6. The incident x-rays are π polarized; for polarization analysis, a graphite crystal is mounted on the detector arm of the diffractometer. The scattering angle of the graphite (006) Bragg reflection is very close to 90° at the photon energy corresponding to the Ho L_{III} absorption threshold of about 8 keV. Scattering at 90° produces a complete linear polarization of the scattered light [65], since no intensity is scattered in the direction parallel to the photon $\underline{E}$ vector
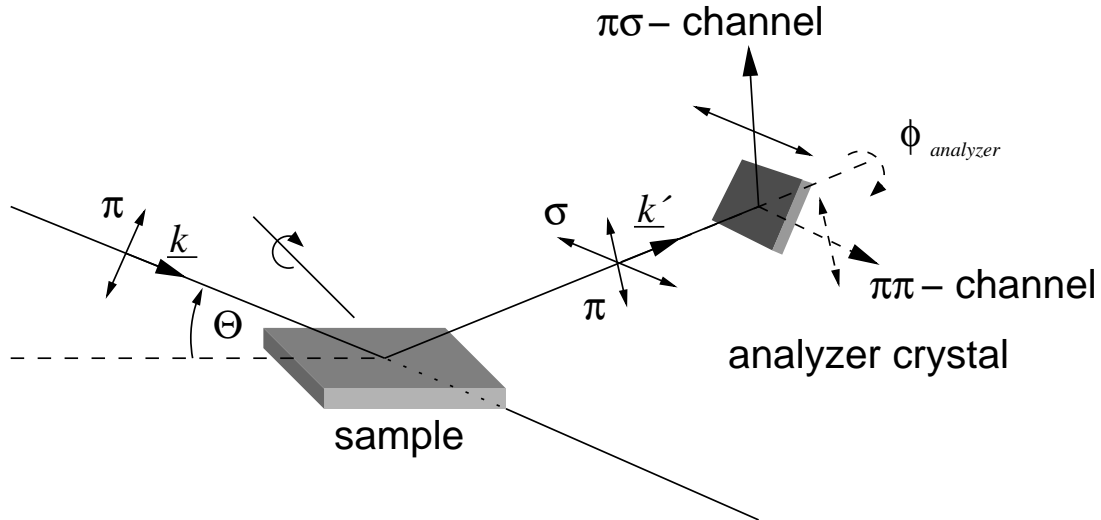
Figure 2.6: Scattering geometry as used in the conventional x-ray experiments performed in this work at the ESRF. The incident π polarized beam is reflected in specular geometry. The scattered beam has two polarization components arising from charge and magnetic scattering. By use of an analyzer crystal with a Bragg angle of 90° at the given photon energy either the π or the σ component of the scattered x-rays can be selected.

(dipole characteristic). Only the component polarized perpendicular to the direction of observation is reflected into the detector, while the other one is suppressed. By rotating the analyzer crystal around the direction of observation ($\phi_{analyzer}$) either the $\pi\pi$ (charge and magnetic scattering) or the $\pi\sigma$ channel (magnetic scattering) can be detected.

The efficiency of polarization analysis is illustrated in figure 2.7. The scans show the region of the (002) Bragg peak of a 113-ML Ho film along the (00l) direction. Without polarization analysis (upper spectrum), no signal from the magnetic superstructure is observable due to the strong background caused by Laue oscillations. The lower spectrum was recorded in the $\sigma\pi$ polarization channel after mounting the graphite (006) analyzer crystal. Applying polarization analysis leads to a suppression of the charge scattering by a factor of about 500, and the magnetic-superstructure satellites (002$\pm\tau$) become clearly visible [53, 90].
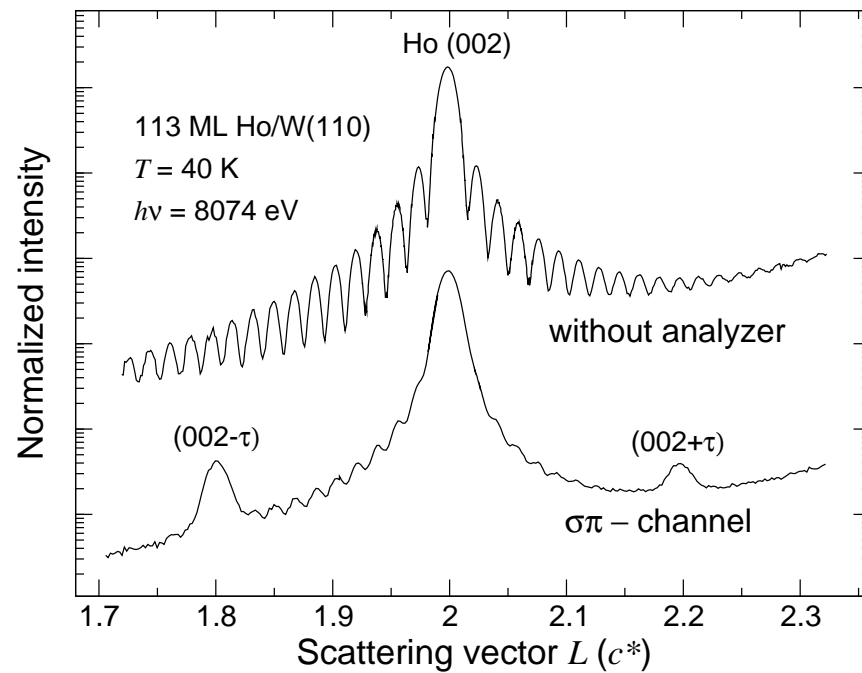
Figure 2.7: Specular x-ray scattering from a 113-ML Ho film at the Ho L_{III} absorption threshold demonstrating the effect of polarization analysis. The incident x-ray beam was chosen to be σ polarized. The top spectrum was recorded without analyzer, showing the Laue profile of the Ho(002) Bragg peak along the surface normal. The spectrum below shows the same scan using polarization analysis. In the $\sigma\pi$ channel the magnetic-superstructure satellites are clearly visible, because the charge-scattering background is suppressed.